FISEVIER

Contents lists available at ScienceDirect

Nuclear Inst. and Methods in Physics Research, A

journal homepage: www.elsevier.com/locate/nima



Full Length Article



Performance of newly constructed plastic scintillator barrel in the WASA-FRS experiments and evaluation of radiation damage effects on multi-pixel photon counter

```
Y.K. Tanaka 1, R. Sekiya 2,3,4, K. Itahashi 2,3,0,a, H. Alibrahim Alfaki 5, F. Amjad 5, M. Armstrong 5,6, K.-H. Behr 5, J. Benlliure 7, Z. Brencic 8,9, T. Dickel 5,10, V. Drozd 5,11, S. Dubey 5, H. Ekawa 1, S. Escrig 12, M. Feijoo-Fontán 7, H. Fujioka 13, Y. Gao 1,14,15, H. Geissel 5,10,c, F. Goldenbaum 16, A. Graña González 7, E. Haettner 5, M.N. Harakeh 11, Y. He 1,17, H. Heggen 5, C. Hornung 5, N. Hubbard 5,18, M. Iwasaki 2,3, N. Kalantar-Nayestanaki 11, A. Kasagi 1,19, M. Kavatsyuk 11, E. Kazantseva 5, A. Khreptak 20,21, B. Kindler 5, H. Kollmus 5, D. Kostyleva 5, S. Kraft-Bermuth 22, N. Kurz 5, E. Liu 1,14,15, B. Lommel 5, S. Minami 5, D.J. Morrissey 23, P. Moskal 21,24, I. Mukha 5, M. Nakagawa 1, C. Nociforo 5, H.J. Ong 15,25,26, S. Pietri 5, S. Purushothaman 5, C. Rappold 12, E. Rocco 5, J.L. Rodríguez-Sánchez 7,27, P. Roy 5, A. Ruber 28, T.R. Saito 1,5,17, S. Schadmand 5, C. Scheidenberger 5,10, P. Schwarz 5, V. Serdyuk 16, M. Skurzok 21,24, B. Streicher 5, K. Suzuki 5,29, B. Szczepanczyk 5, X. Tang 14, N. Tortorelli 5, M. Vencelj 8, T. Weber 5, H. Weick 5, M. Will 5, K. Wimmer 5, A. Yamamoto 3, A. Yanai 1,31, J. Zhao 5,32,5, for WASA-FRS / Super-FRS Experiment Collaboration
```

https://doi.org/10.1016/j.nima.2025.171065

¹ High Energy Nuclear Physics Laboratory, RIKEN Cluster for Pioneering Research, RIKEN, 351-0198, Wako, Saitama, Japan

² Meson Science Laboratory, RIKEN Cluster for Pioneering Research, RIKEN, 351-0198, Wako, Saitama, Japan

³ Nishina Center for Accelerator-Based Science, RIKEN, 351-0198, Wako, Saitama, Japan

⁴ Kyoto University, 606-8502, Kyoto, Japan

⁵ GSI Helmholtzzentrum für Schwerionenforschung GmbH, 64291, Darmstadt, Germany

⁶ Institut für Kernphysik, Universität Köln, 50923, Köln, Germany

⁷ IGFAE, Universidade de Santiago de Compostela, 15782, Santiago de Compostela, Spain

⁸ Jožef Stefan Institute, 1000, Ljubljana, Slovenia

⁹ University of Ljubljana, 1000, Ljubljana, Slovenia

¹⁰ Universität Gießen, 35392, Gießen, Germany

¹¹ ESRIG, University of Groningen, 9747 AA, Groningen, The Netherlands

¹² Instituto de Estructura de la Materia - CSIC, 28006, Madrid, Spain

¹³ Institute of Science Tokyo, 152-8551, Tokyo, Japan

¹⁴ Institute of Modern Physics, Chinese Academy of Sciences, 730000, Lanzhou, China

¹⁵ School of Nuclear Science and Technology, University of Chinese Academy of Sciences, 100049, Beijing, China

¹⁶ Institut für Kernphysik, Forschungszentrum Jülich, 52425, Jülich, Germany

¹⁷ Lanzhou University, 730000, Lanzhou, China

¹⁸ Institut für Kernphysik, Technische Universität Darmstadt, 64289, Darmstadt, Germany

¹⁹ Graduate School of Engineering, Gifu University, 501-1193, Gifu, Japan

²⁰ INFN, Laboratori Nazionali di Frascati, 00044, Frascati, Roma, Italy

²¹ Institute of Physics, Jagiellonian University, 30-348, Kraków, Poland

²² TH Mittelhessen University of Applied Sciences, 35390, Gießen, Germany

²³ National Superconducting Cyclotron Laboratory, Michigan State University, MI 48824, East Lansing, USA

²⁴ Center for Theranostics, Jagiellonian University, 30-348, Kraków, Poland

^{*} Corresponding author.

E-mail address: yoshiki.tanaka@a.riken.jp (Y.K. Tanaka).

^a Present address: Department of Physics, The University of Osaka, 560-0043, Osaka, Japan.

^b Present address: Auburn University, Auburn, AL, 36832, USA.

c Deceased.

^d Present address: Variable Energy Cyclotron Centre, Kolkata, 700064, India.

- ²⁵ Joint Department for Nuclear Physics, Lanzhou University and Institute of Modern Physics, Chinese Academy of Sciences, 730000, Lanzhou, China
- ²⁶ Research Center for Nuclear Physics, Osaka University, 567-0047, Osaka, Japan
- ²⁷ CITENI, Campus Industrial de Ferrol, Universidade da Coruña, 15403, Ferrol, Spain
- ²⁸ Uppsala University, 75220, Uppsala, Sweden
- ²⁹ Ruhr-Universität Bochum, Institut für Experimentalphysik I, 44780, Bochum, Germany
- ³⁰ KEK, 305-0801, Tsukuba, Ibaraki, Japan
- 31 Saitama University, 338-8570, Saitama, Japan
- 32 Peking University, 100871, Beijing, China

ARTICLE INFO

Keywords: Silicon photomultiplier MPPC Plastic scintillator Timing counter Radiation damage High counting rate performance

ABSTRACT

A barrel-shaped plastic scintillation counter with Multi-Pixel Photon Counter (MPPC) readout has been developed and operated in the first WASA-FRS experimental campaign at GSI. The detector was used to measure charged particles emitted from reactions induced by a 2.5 GeV proton beam incident on a carbon target, providing particle identification in combination with momentum reconstruction in a 1 T magnetic field. The performance of this detector, particularly its response to energy deposition and time resolution, was systematically investigated as a function of count rate and total number of irradiating protons. A time resolution of 45–75 ps (σ) , depending on the energy deposition, was achieved. Stable performance was maintained under high-rate conditions up to 1.35 MHz per single counter, with no significant degradation in either signal amplitude or timing response. Radiation-induced damage to the MPPCs was observed primarily as a reduction in signal amplitude, with approximately 35% decrease at an estimated 1 MeV neutron-equivalent fluence of 2.4×10^{10} cm⁻².

1. Introduction

In recent years, silicon photomultipliers, also referred to as Multi-Pixel Photon Counters (MPPCs), have been widely adopted as readout detectors for scintillation counters in particle- and nuclear-physics experiments. Their advantages lie in their compactness, lower cost, and insensitivity to magnetic fields, compared to conventional readout systems using photomultiplier tubes. These features make MPPCs suitable readout devices for plastic scintillators as part of particle identification detectors within spectrometer systems, where the plastic materials are placed in strong magnetic fields and often in limited spaces. High time resolution can be achieved by coupling MPPCs with fast-timing plastic scintillators, owing to the intrinsically fast timing response of MPPCs [1–7].

However, one of the potential issues with MPPC readout is its limited radiation tolerance. It has been reported that radiation damage in silicon sensors leads to an increase of leakage currents, higher dark count rates, and a reduction in signal amplitude under exposure to various types of irradiation [8–15]. These effects can become critical, particularly in experiments involving hadronic beams, where high neutron fluences are expected within relatively short time periods. Therefore, it is of particular importance to investigate and characterize the performance not only of the sensors themselves, but also of the full MPPC-based scintillator system, in terms of particle reconstruction capabilities under realistic experimental conditions, when it is integrated within a full spectrometer setup.

We developed a plastic scintillator system based on MPPC readout [16] as a part of the Wide-Angle Shower Apparatus (WASA) spectrometer system [17,18] and operated it in the first series of the WASA-FRS experiments at GSI [19,20]. The detector was employed for the identification of charged particles emitted from proton- and heavyion-induced reactions, by measuring their time of flight and the energy deposition in combination with momentum reconstruction performed using tracking detectors inside a 1 T solenoidal magnetic field. Two experiments were carried out in the first experimental campaign, one on the spectroscopy of η' -mesic nuclei [21,22] and the other on light hypernuclear spectroscopy using heavy-ion-induced reactions [23].

In this article, we report on a systematic investigation of the performance of the newly constructed plastic scintillator barrel from the analysis of the spectroscopy experiment of η' -mesic nuclei. The detector response to energy deposition and the time resolution were analyzed under various conditions, including dependence on the counting rate

and the total number of irradiating protons for evaluating radiation tolerance. The structure of this paper is as follows. First, the experimental setup and measurements are introduced in Section 2. The data-analysis procedure is presented in Section 3, followed by results and discussions in Section 4. Finally, the conclusions are summarized in Section 5.

2. Experiment

The experimental setup for the spectroscopy of η' -mesic nuclei is illustrated in Fig. 1. The central part of the WASA detector was installed at the F2 focal plane of the fragment separator FRS [24]. We employed a 2.5 GeV proton beam extracted from the SIS-18 synchrotron in a slow extraction mode with a spill length of 10 s and a cycle of 11 s. The beam impinged on a carbon target placed at F2 to produce η' -mesic nuclei with the $^{12}\text{C}(p,d)\eta'\otimes^{11}\text{C}$ reaction. A typical rate of the proton beam on the target was $\sim 5\times 10^8/\text{s}$, and the spot size of the beam was about 1 mm (σ) in both horizontal and vertical directions. The carbon target had a cylindrical shape with a radius of 1.5 cm and was aligned with the beam axis and installed inside the WASA detector at a position 15 cm downstream of the detector's central point. The areal density of the target was 4 g/cm² along the beam axis.

The F2–F4 section of the FRS was operated as a high-resolution momentum spectrometer at a magnetic rigidity of 9.4 Tm. Forward-emitted deuterons from the $^{12}\mathrm{C}(p,d)$ reaction near the η' -meson production threshold were identified by time-of-flight measurements between the plastic scintillators installed at F3 and F4. Their momenta were reconstructed from trajectories measured with the multi-wire drift chambers at F4, yielding a momentum resolution of $\sigma_P/P\sim 1/3000$, and were then used to calculate the missing mass of the (p,d) reaction. Further details on the particle identification at the FRS and on the tracking detectors can be found in Refs. [19,25].

The WASA central detector was used to measure and tag particles emitted from the decay of the η' -mesic nuclei, in order to enhance the signal-to-background ratio of the spectrum [26] compared to the previous experiment [25,27]. As shown in the lower panel of Fig. 1, the WASA detector is a spectrometer system consisting of several components: a mini-drift chamber (MDC) [28], a plastic scintillator barrel (PSB) and forward and backward end caps (PSFE and PSBE, respectively), a superconducting solenoid magnet [29], and a scintillator electromagnetic calorimeter (SEC) [30]. Momenta of charged particles were reconstructed from their trajectories in a magnetic field of 1 T, measured by the MDC. The plastic scintillators provided timing and energy-deposition measurements, and contributed to particle identification in combination with the momentum information from the MDC.

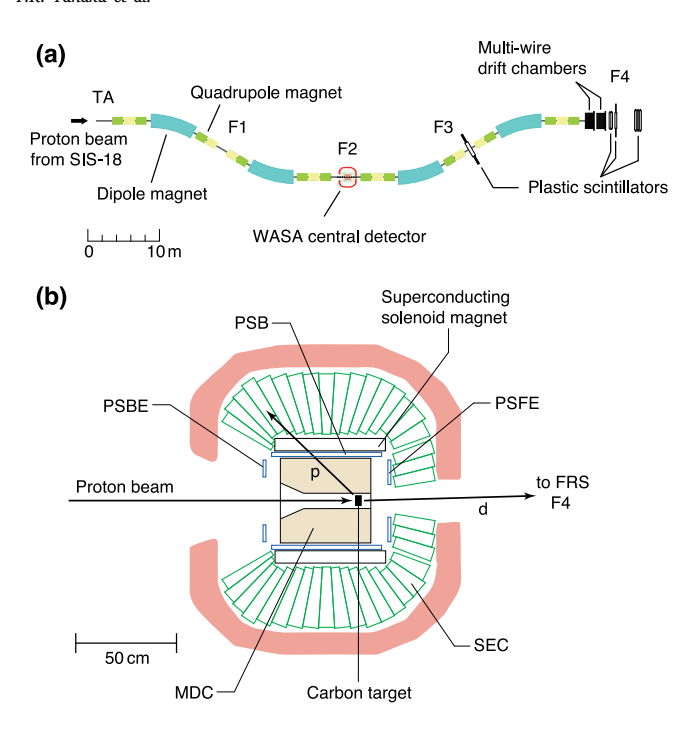


Fig. 1. (a) A schematic experimental setup with the WASA central detector and the FRS at GSI. A 2.5 GeV proton beam impinged on a carbon target at F2. Deuterons emitted in the (p,d) reaction were analyzed by the F2–F4 section of FRS. Decay particles from η' -mesic nuclei were detected by the WASA detector at F2. (b) A schematic configuration of the WASA central detector at F2. A carbon target was installed at 15 cm downstream position from the central point of the WASA detector. Emitted particles from reactions were measured by the MDC, PSB, PSFE, PSBE, and SEC detectors. See text for details of these detectors.

The SEC was used to detect high-energy photons emitted from the decay of neutral mesons.

In this article, we focus on the analysis of the PSB detector, which was newly developed and constructed for the present experiment [16]. A schematic view of the PSB is shown in Fig. 2. The detector consists of 46 plastic scintillation bars, each with dimensions of $550 \times 38 \times 8$ mm³, arranged in a cylindrical barrel configuration. The bars were alternately positioned at radial distances of 221 mm and 232 mm from the central beam axis, with a step in azimuthal angle of $\Delta \phi = 7.35^{\circ}$, making overlapping regions between the adjacent bars of approximately 9 mm. The entire azimuthal angle range was covered, except for regions $85.85^{\circ} \le \phi \le 94.15^{\circ}$ and $265.85^{\circ} \le \phi \le 274.15^{\circ}$ due to the support structure. Eljen Technology EJ-230 was used as the scintillator material, which has an attenuation length of 120 cm and rise and decay times of 0.5 ns and 1.5 ns, respectively. All side surfaces of the scintillator bars were covered with reflective aluminum foil.

The MPPC S13360-6050PE manufactured by Hamamatsu Photonics was employed as the photon detector. It has a photosensitive area of 6×6 mm² and a pixel pitch of 50 µm. Three MPPCs were electrically connected in series on a printed circuit board and directly attached to both the upstream and downstream ends of the scintillator bar with respect to the beam direction, covering approximately 36% of the readout surface area. An optical grease TSK5353 (Momentive Performance Materials) was used to optically couple the plastic bars to the MPPCs. On the readout surface of the bar, the regions not coupled to the MPPCs were left uncovered and exposed to air. Each MPPC was operated at a bias voltage of 55.0 V, corresponding to an overvoltage of 3.5 V. The bias voltage was supplied using a regulated power supply (PMX250-0.25A) manufactured by Kikusui Electronics.

Raw signals from the MPPCs were transmitted via 7 m-long CLF100 coaxial cables to amplifier modules based on the design reported in

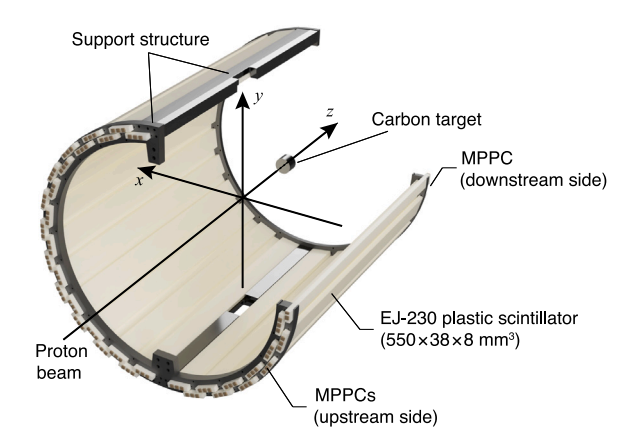


Fig. 2. A three-quarter section view of the PSB and the location of the carbon target. 46 slats of plastic scintillator (EJ-230) with dimensions of $550 \times 38 \times 8 \text{ mm}^3$ were alternately positioned at radial distances of 221 mm and 232 mm from the central beam axis, with overlapping regions between adjacent bars. Three MPPCs (S13360-6050PE) were attached to both the upstream and downstream ends of the scintillator bar with respect to the beam direction. The center of the plastic bar was positioned at z=0 mm, while the target was installed at z=150 mm.

Ref. [1]. Two modifications were introduced to meet the requirements of the present experiment. First, the total resistance of the low-pass filter circuit used for feeding the bias voltage was reduced from 3.6 k Ω to 110 Ω to improve high-rate performance. Second, the Π -type attenuator was modified to match the expected signal amplitudes to the dynamic range of the subsequent readout electronics. The amplified signals were digitized using a CAEN V1742 waveform digitizer operating at a sampling rate of 2.5 GHz for timing and amplitude analysis. Split signals were also sent to a constant-fraction discriminator (MCFD-16, Mesytec GmbH), and the coincidence rate of the signals between the upstream and downstream MPPCs was recorded using a 250 MHz scaler (CAEN V830).

The intensity of the primary proton beam was continuously monitored during the experiment using a Secondary Electron Transmission Monitor (SEETRAM) [31], installed at the standard target area (TA) of the FRS. The current signal from the SEETRAM was converted into a pulse frequency using a current digitizer (GSI CD1011) and recorded with the CAEN V830 scaler. The SEETRAM response was calibrated for 2.5 GeV protons at the end of this experiment, with an accuracy of approximately 5%.

The data-acquisition system was triggered by several conditions. The primary trigger was generated by a time-of-flight-based coincidence of scintillator signals from F3 and F4 of the FRS, enabling efficient recording of events associated with the $(p,\ d)$ reaction. In addition, a downscaled signal from the F4 scintillator alone, with a factor of 128, was added to the trigger logic to record a fraction of the $(p,\ p')$ reaction events. Downscaled signals from the PSB, PSBE, and PSFE detectors, with factors of 2^{13} – 2^{14} , as well as a 5 Hz clock signal, were also included for calibration purposes. In the following sections, data collected under all trigger conditions were combined and analyzed.

3. Data analysis

Waveform data of the PSB signals were analyzed to extract the hit timing and energy deposition of charged particles. A software-based method of a constant-fraction discriminator [32] was employed to define the hit timing while suppressing time-walk effects. We adopted a delay parameter of $2.8~\rm ns$ and a fraction parameter of $0.4~\rm by$ optimizing the resulting time resolution. The energy deposition was evaluated by integrating baseline-subtracted waveform within a time window of [-4,

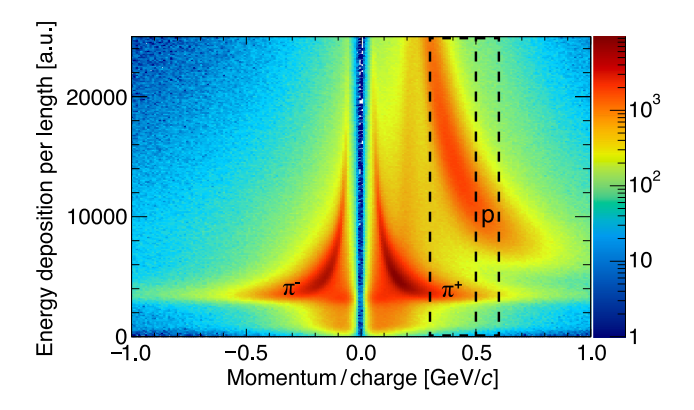


Fig. 3. A typical example of a particle identification plot. The abscissa shows the reconstructed momentum divided by the sign of the charge, as obtained from the track fitting analysis. The ordinate shows the energy deposition per unit track length in the PSB volume. Boxes with the dashed lines indicate the selected momentum regions used for analyzing the QDC response and time resolution.

20] ns relative to the point where the signal crossed a fixed threshold of -12 mV. Since this procedure emulates the function of a charge-to-digital converter (QDC), the resulting quantity is hereafter referred to as the QDC value. These analyses were performed for the MPPC readouts at both the upstream and downstream ends of each scintillator bar. The hit timing of the PSB slat was then determined as the arithmetic mean of the timings from both ends, while the energy deposition was calculated as the geometric mean of the two QDC values, in order to eliminate dependence on the longitudinal hit position (z).

The momentum and trajectory of charged particles were reconstructed by fitting drift-length data measured by the MDC. First, an elastic-arm algorithm [33] was applied to select a combination of hits forming each trajectory. The selected hits were then fitted by employing a Kalman-filter algorithm with the GENFIT toolkit [34]. The position resolution of each MDC layer was estimated to be $\sim 200~\mu m~(\sigma)$, resulting in a typical momentum resolution of approximately 15% at 0.5 GeV/c. Details of the MDC analysis will be reported elsewhere [35].

Charged particles were identified by combining the reconstructed momentum and the measured energy deposition. Fig. 3 shows an example of a particle identification plot. The horizontal axis represents the reconstructed momentum divided by the charge, while the vertical axis shows the energy deposition divided by the track length within the PSB volume, as evaluated from the track fitting analysis. Data from all PSB slats were combined after applying individual time offset and gain corrections. Protons (p) and charged pions (π^{\pm}) are clearly distinguished, as demonstrated in the figure. It should be mentioned that the nearly vertical band at the momentum divided by the charge around $0.2~{\rm GeV}/c$ is caused by the stopped protons inside the PSB.

The response to the energy deposition was analyzed using QDC spectra obtained from the individual upstream and downstream MPPCs, as well as from their geometric mean. Two momentum regions were selected for this analysis: 0.3–0.5 GeV/c and 0.5–0.6 GeV/c, as illustrated in Fig. 3. The former was used to analyze positive pions corresponding to minimum ionizing particles, while the latter was for protons with approximately 3 times higher energy depositions. We further selected the longitudinal hit position within 100 mm $\leq z \leq$ 200 mm for the energy-deposition analysis in order to reduce the effect of light attenuation along the z-direction in the QDC spectra of the individual upstream and downstream MPPCs.

Fig. 4 shows examples of the QDC spectra for one of the PSB slats. The π^+ peak observed in the momentum range of 0.3–0.5 GeV/c was fitted with an empirical function of the form $f(x) = p_0 \exp{(-(x-p_1)^2/(p_2+p_3x)^2)} + (p_4+p_5x)$, where the first term represents an asymmetric peak structure, and the second term accounts for the

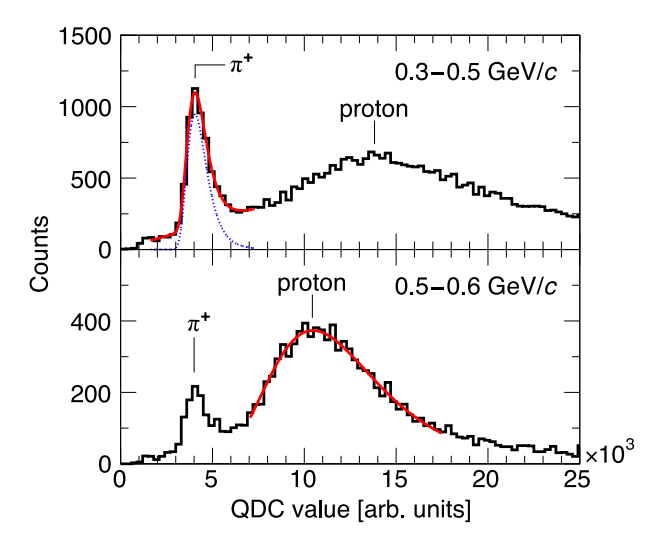


Fig. 4. Examples of QDC spectra for the momentum ranges of 0.3–0.5 GeV/c (upper panel) and 0.5–0.6 GeV/c (lower panel). The geometric mean of the QDC values from the upstream and downstream MPPCs was plotted. The red solid curves represent fit functions (see text for details). The blue dotted curve in the upper panel shows the peak component of the fit function.

continuous background arising from the tail of the proton peak. In contrast, the proton peak in the 0.5– $0.6~{\rm GeV}/c$ range was well reproduced using only the first term, as the pion contribution in this region was sufficiently small. The peak position and the full width at half maximum (FWHM) were extracted to characterize the PSB response in terms of energy deposition.

The time resolution of the PSB was evaluated for the inner slats by using tracks penetrating the overlapping region between the inner and outer PSB slats. Two data sets, one for π^+ in the momentum range of 0.3–0.5 GeV/c and the other for protons in 0.5–0.6 GeV/c, were selected based on the momentum and QDC values. In addition, the longitudinal hit position in a range of $-25~\text{mm} \leq z \leq 25~\text{mm}$ was selected, except when scanning the z-dependence of the resolution.

We defined the following three quantities for evaluating the time resolution:

$$T_{\text{1UD}} = T_{\text{1U}} - T_{\text{1D}} - f \cdot z \tag{1}$$

$$T_{1U2} = T_2 - T_{1U} + \frac{f \cdot z}{2} \tag{2}$$

$$T_{\rm 1D2} = T_2 - T_{\rm 1D} - \frac{f \cdot z}{2}.$$
 (3)

Here, $T_2 = (T_{2U} + T_{2D})/2$, and T_{ij} (i = 1, 2 and j = U, D) represents the hit timing measured at the upstream (j = U) or downstream (j = D) MPPCs of the inner (i = 1) or outer (i = 2) PSB slat, which was defined relative to the common reference time based on the trigger signal measured by each of the waveform digitizer modules. z denotes the longitudinal hit position at the inner PSB slat, obtained from track fitting. The terms with a factor f were introduced to compensate for z dependence of T_{1U} and T_{1D} due to the light propagation time inside the scintillator bar, which can be expressed as $(z-z_{\rm U})/v_{\rm eff}$ and $(z_{\rm D}-z)/v_{\rm eff}$ for $T_{\rm 1U}$ and T_{1D} , respectively. Here, $v_{\rm eff}$ represents the effective propagation speed of light inside the scintillator bar along the z direction, and $z_{\rm U} = -275$ mm and $z_{\rm D} = 275$ mm denote the z positions of the upstream and downstream readout surfaces, respectively. It should be noted that T_2 does not have such z dependence, since it is defined by averaging $T_{2\mathrm{U}}$ and $T_{2\mathrm{D}}$. The factor $f=2/v_{\mathrm{eff}}$ was determined to be $f = 14.8 \pm 0.1$ ps/mm by fitting observed correlations in the data. Each of the distributions defined by Eqs. (1)-(3) exhibits a peak structure. The width of each peak (σ) was extracted by fitting it with a Gaussian function. All combinations of the two overlapping PSB slats were used for this analysis, with individual time offsets corrected.

The obtained widths ($\sigma_{1\text{UD}}$, $\sigma_{1\text{U2}}$, and $\sigma_{1\text{D2}}$) can be related to the individual time resolutions of $T_{1\text{U}}$, $T_{1\text{D}}$, and T_{2} ($\sigma_{1\text{U}}$, $\sigma_{1\text{D}}$, and σ_{2} , respectively) by the following equations:

$$\sigma_{\text{IUD}}^2 = \sigma_{\text{IU}}^2 + \sigma_{\text{ID}}^2 + f^2 \sigma_z^2 \tag{4}$$

$$\sigma_{1U2}^2 = \sigma_{1U}^2 + \sigma_2^2 + \frac{f^2 \sigma_z^2}{4}$$
 (5)

$$\sigma_{1D2}^2 = \sigma_{1D}^2 + \sigma_2^2 + \frac{\sigma^2 \sigma_z^2}{4}.$$
 (6)

Note that σ_z can be obtained from the track fitting analysis. Therefore, Eqs. (4)–(6) can be solved to determine $\sigma_{1\mathrm{U}}$, $\sigma_{1\mathrm{D}}$, and σ_2 . The time resolution of the inner slat σ_1 can be obtained as well by $\sigma_1 = \sqrt{\sigma_{1\mathrm{U}}^2 + \sigma_{1\mathrm{D}}^2}/2$, since the hit time at the inner slat is defined as $T_1 = (T_{1\mathrm{U}} + T_{1\mathrm{D}})/2$.

The QDC response and time resolution were systematically analyzed as functions of both the count rate and the total number of irradiating protons. The count-rate dependence was studied to investigate performance under high-rate conditions, using scaler information within a time window of [-100, 0] ms relative to each hit. In contrast, the dependence on the total number of incident protons was analyzed in order to evaluate possible radiation damage effects. The total number of protons was determined by integrating the SEETRAM current from the start of the production measurements. In this experiment, a total of 1.1×10^{14} protons impinged on the target. Long-term radiation effects were analyzed by dividing the entire data into 11 subsets, each corresponding to 0.1×10^{14} incident protons.

4. Results and discussions

4.1. Results of QDC analysis

Analyzed peak values of the QDC are presented in Fig. 5 to illustrate the dependence on the count rate. Data sets corresponding to $\sim 20\%$ of the total incident protons were used in the analysis of the rate dependence. The QDC values were normalized to those obtained at the lowest count rate for each of the data sets: π^+ in the 0.3–0.5 GeV/c range and proton in the 0.5–0.6 GeV/c range. The spectra of all PSB slats were combined after normalizing each individual spectrum. No significant reduction greater than 2% is observed up to a counting rate of 1.35 \times 10⁶/s. This result demonstrates a substantial improvement compared to the prototype detector previously reported in Ref. [16], where a visible drop of approximately 20% was found already at 1 MHz. The improvement can be attributed to the reduced resistance in the low-pass filter circuit as well as the use of a more stable power supply for biasing the MPPCs in the present experiment.

Obtained widths of the QDC peaks are shown as a function of the count rate in Fig. 6. The widths are normalized to the corresponding QDC peak values under each condition. The observed widths remain stable over the entire range of count rates, taking values in the range of 0.31–0.36 for the π^+ data set and 0.61–0.78 for the proton data set. This also represents a significant improvement compared to the results of the prototype detector [16].

The long-term trends of the QDC response are shown in Fig. 7 as functions of the total number of protons N_p impinging on the carbon target. The analysis was performed per slat, and the averaged values over all slats are presented. Each plot of the QDC values in the upper panel is normalized to unity at the extrapolated value for $N_p=0$. The QDC value based on the geometric mean decreased to 76%, primarily due to the QDC of the downstream MPPC which dropped to 63%–65%, while that of the upstream MPPC dropped only to 90%–91%. The observed slope of the reduction is the same for the π^+ (0.3–0.5 GeV/c) and proton (0.5–0.6 GeV/c) data sets. The variations of the normalized QDC values among the different PSB slats were about 0.02, 0.03, and 0.02 in standard deviation for the upstream MPPCs (U), the downstream MPPCs (D), and their geometric mean (M),

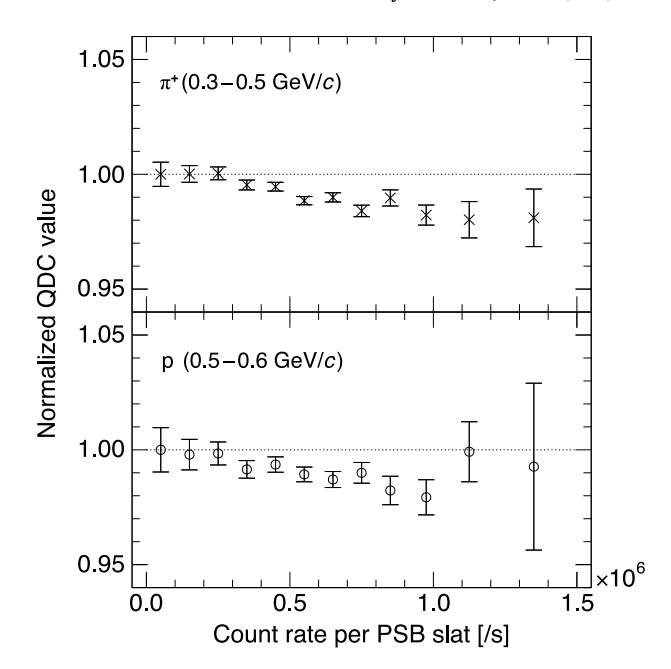


Fig. 5. Normalized QDC values as a function of the counting rate per individual PSB slat. The geometric mean of the QDC values from the upstream and downstream MPPCs was used. The QDC values were normalized to the first data point, which corresponds to the lowest rate of 5×10^4 counts/s.

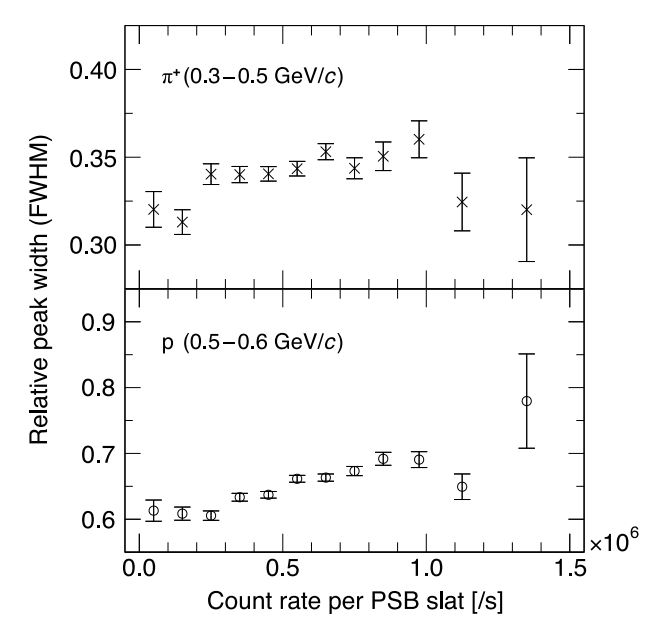


Fig. 6. Relative peak widths (FWHM) of QDC as a function of the counting rate per individual PSB slat. The geometric mean of the QDC values from the upstream and downstream MPPCs was used.

respectively, at $N_p=1.05\times 10^{14}$. In contrast, widths of the QDC peaks remain stable over the entire irradiation time, as shown in the lower panel of Fig. 7.

The observed reduction of the QDC values can be attributed to effects due to radiation damage of the MPPCs, since the downstream MPPCs are located closer to the reaction target. It should be noted that the plastic scintillator material may also suffer from radiation damage, which should introduce dependence of the reduction slopes on the longitudinal hit position z. We examined such z dependence by repeating the analysis selecting different z regions and obtained reduction slopes consistent with those shown in Fig. 7. These results

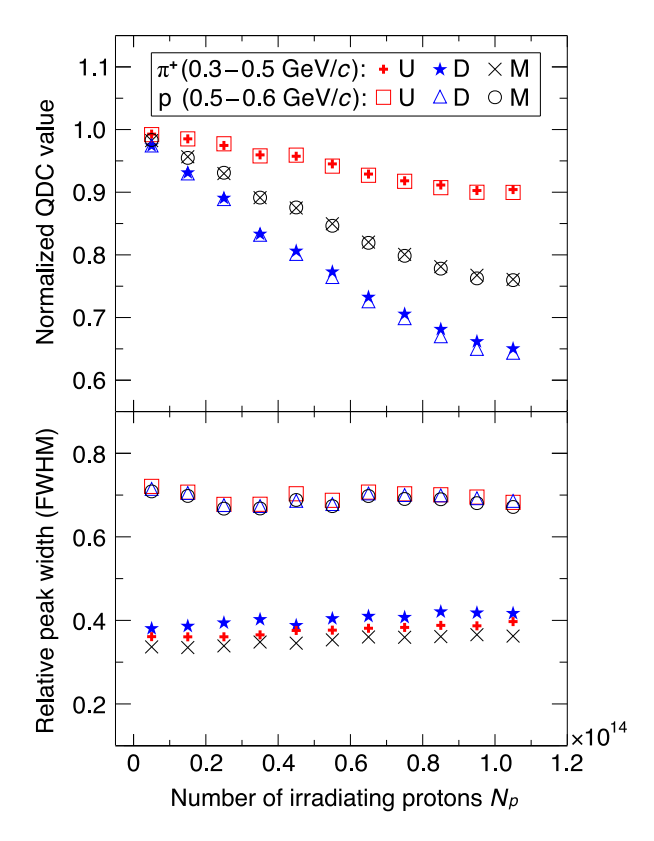


Fig. 7. Normalized software QDC values (upper panel) and relative peak widths (lower panel) as functions of the total number of irradiating protons, N_p . Results based on the upstream MPPCs (U), the downstream MPPCs (D), and their geometric mean (M) are shown in red, blue, and black, respectively. The QDC values were normalized to unity at the extrapolated values for $N_p = 0$.

therefore indicate that the observed reductions are mainly due to radiation damage of the MPPCs.

The number of protons on target can be translated into the 1 MeV neutron-equivalent fluence at each position of the upstream and downstream MPPCs. For this estimation, a Monte-Carlo simulation was performed using the Geant4 framework [36] to first evaluate the energy- and particle-dependent fluences at the MPPC locations. The FTFP_BERT_HP physics list of the Geant4 was employed [37], which incorporates high-precision neutron models and cross sections at low energies. The resulting fluences of neutrons and protons for 10⁹ incident protons are shown in Fig. 8. Contributions of other particles such as π^{\pm} and e^{\pm} were negligibly small compared to those by the neutrons and protons. The obtained spectra of all these particles were then integrated with the corresponding NIEL (Non-Ionizing Energy Loss) scaling factors in silicon [38] normalized to the value for 1 MeV neutron [39]. As a result, the 1 MeV neutron-equivalent fluences per 109 incident protons were estimated to be 3.8×10^4 cm⁻² and 2.3×10^5 cm⁻² at the upstream and downstream MPPC positions, respectively.

Fig. 9 shows the reduction of the QDC values as a function of the 1 MeV neutron-equivalent fluence. The reductions observed in the upstream and downstream MPPCs follow a consistent trend in terms of the 1 MeV neutron-equivalent fluence, indicating that the equivalent fluence serves as a suitable index to characterize the amplitude reduction of the MPPCs. The largest reduction observed in the present data is 35%–37% at a total fluence of 2.4×10^{10} cm⁻². This level of degradation is consistent in magnitude with results reported in Refs. [9,10].

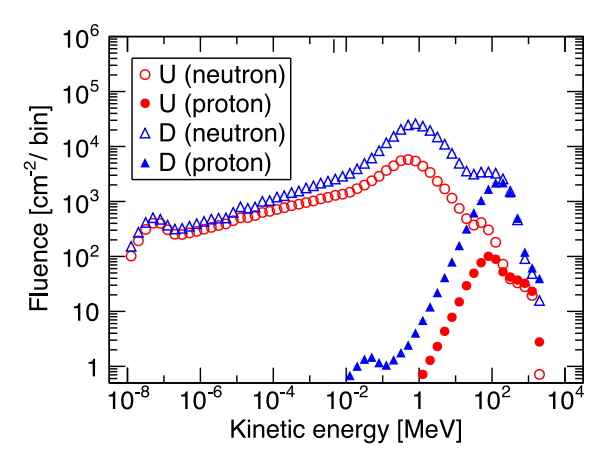


Fig. 8. Simulated non-weighted fluences of protons and neutrons at the locations of the upstream (U) and downstream (D) MPPCs, assuming 10^9 incident protons on a 4 g/cm² carbon target.

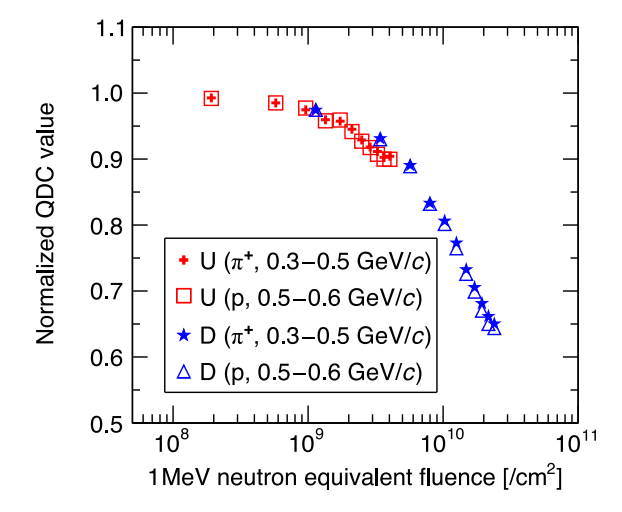


Fig. 9. Normalized QDC values as a function of the integrated 1 MeV neutron-equivalent fluence in silicon. The QDC values were normalized in the same manner as in Fig. 7.

4.2. Results of time-resolution analysis

The analyzed position dependence of the time resolution is shown in Fig. 10 for π^+ in the momentum range of 0.3–0.5 GeV/c and for protons of 0.5–0.6 GeV/c. The achieved time resolutions σ_1 exhibit a moderate dependence on z, with values in the ranges of 74–80 ps and 42–54 ps (σ) for the π^+ and proton data, respectively. In contrast, the individual contributions from the upstream and downstream MPPCs (σ_U and σ_D) show a clear dependence on the hit position z, which can be understood in terms of light attenuation and differences in photon path length. It should be noted that the particle track length in the plastic bar is correlated with the hit position, as the target is located at z=150 mm and the center of the PSB at z=0 mm. The observed asymmetry between $z\leq 0$ mm and 0 mm $\leq z$ in Fig. 10, especially in the proton case, can be understood in this context by different energy deposition, which will be discussed in the following paragraph.

The dependence of time resolution on energy deposition is presented in Fig. 11. The normalization of the energy deposition was performed by fitting the measured QDC–momentum correlation to a Monte Carlo simulation using the Geant4 framework [36]. The time resolution improves as the energy deposition increases, up to approximately 10 MeV, above which it remains nearly constant due to saturation. Each

¹ Geant4 version 10.6.1 was used in the persent simulation.

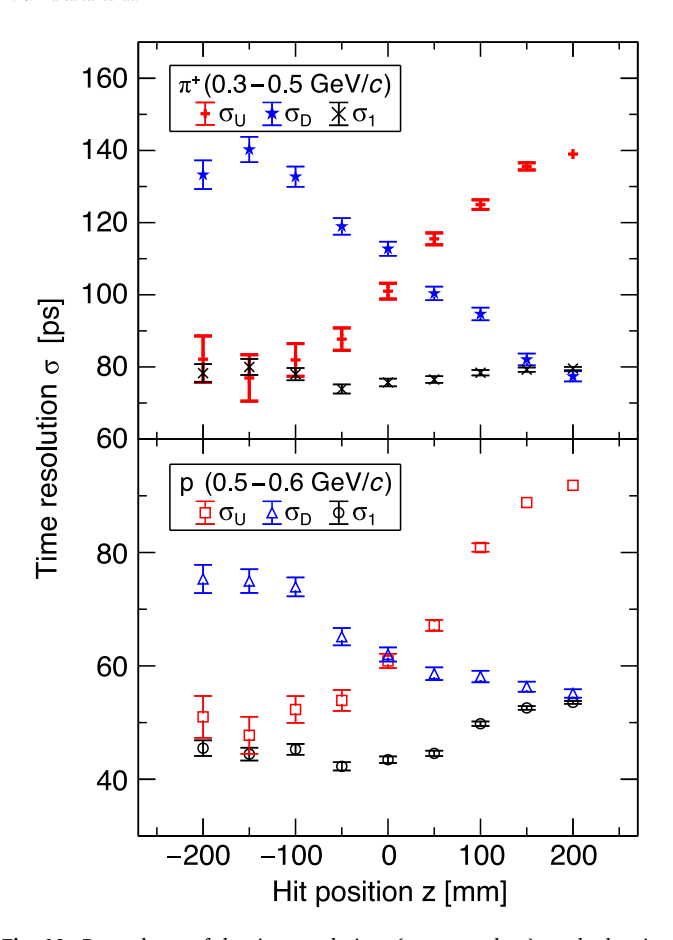


Fig. 10. Dependence of the time resolutions (σ_1 , σ_U , and σ_D) on the longitudinal hit position z for π^+ in the momentum range of 0.3–0.5 GeV/c (upper panel) and for protons of 0.5–0.6 GeV/c (lower panel).

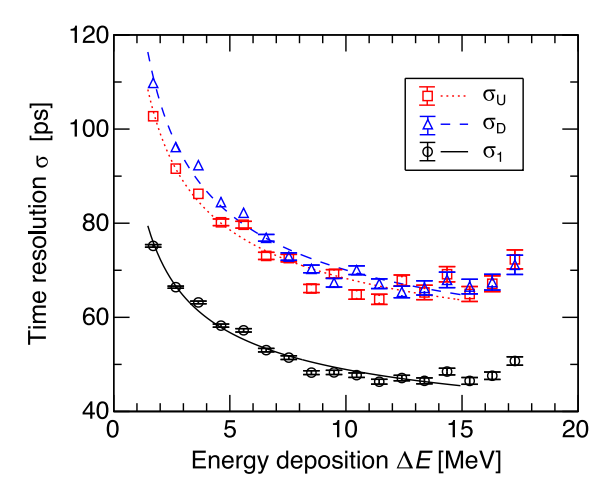


Fig. 11. Dependence of time resolutions on the energy deposition ΔE . The dotted, dashed, and solid curves show fit results with $f(\Delta E) = p_0 + p_1/\sqrt{\Delta E}$. Data sets corresponding to the first 0.1×10^{14} incident protons (the first data points in Fig. 13) were used in this analysis.

time resolution plot can be fitted with an empirical function of the form $f(\Delta E) = p_0 + p_1/\sqrt{\Delta E}$, as shown in the figure.

Fig. 12 shows the analyzed time resolutions σ_1 as a function of the counting rate. The time resolutions remain stable over the entire range of the count rate for both the π^+ and proton data sets. No significant deterioration is observed up to a counting rate of 1.35×10^6 /s per single

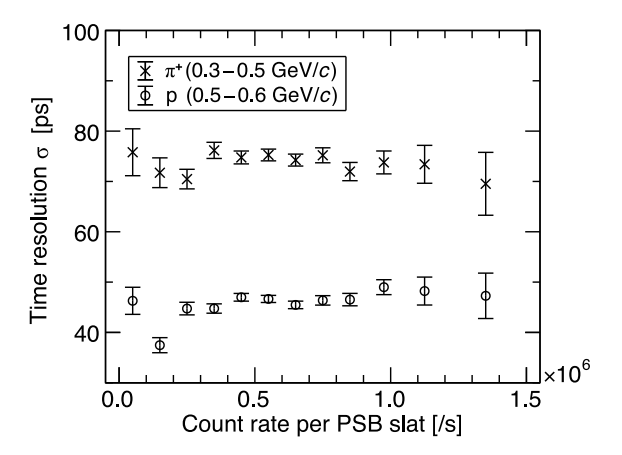


Fig. 12. Dependence of time resolutions on the counting rate per individual PSB slat

slat of the PSB. This demonstrates a substantial improvement in highrate capability, also in terms of the time resolution, compared to the prototype previously reported in Ref. [16].

In Fig. 13, the time resolutions are shown as a function of the total number of protons impinging on the carbon target. The upper and lower panels correspond to the π^+ (0.3–0.5 GeV/c) and proton (0.5–0.6 GeV/c) data sets, respectively. The resolution per slat (σ_1) gradually deteriorates from 76 ps to 83 ps for the π^+ data, and from 43 ps to 46 ps for the proton data, as the total number of the irradiating protons increases. This deterioration is mainly attributed to the downstream MPPCs, as indicated by the decomposed resolution component (σ_D).

The observed increase of the time resolution can be interpreted as a consequence of the reduced signal amplitude, shown in Fig. 7, as follows. We assume and estimate the time resolution $\sigma_i(N_p)$ after irradiation with N_p protons for each component $i=\mathrm{U},\mathrm{D},1$ to be $\sigma_i(N_p)=f_i(R_i(N_p)\cdot f_i^{-1}(\sigma_i(n_0))).$ Here, $n_0=0.05\times 10^{14}$ is the averaged number of protons corresponding to the first data point in Figs. 7 and 13, f_i is the fitted ΔE dependence of the time resolutions in Fig. 11, and $R_i(N_p)$ is the QDC reduction factor at N_p relative to the first point at n_0 in Fig. 7. The estimated trends for $\sigma_{\mathrm{U}},\,\sigma_{\mathrm{D}},\,$ and σ_{I} are presented in Fig. 13 by the dotted, dashed, and solid curves, respectively. The observed increase in time resolution is well reproduced by this estimation, indicating that the degradation is primarily due to the signal amplitude reduction. This implies that no additional deterioration of the intrinsic time resolution of the MPPCs is observed as far as the present data are concerned.

5. Conclusion

In summary, the newly constructed plastic scintillator barrel with multiple-MPPC readout was successfully operated in the first WASA-FRS experiment at GSI. Its performance, specifically the response to energy deposition and the time resolution, was systematically investigated in terms of the dependence on the count rate and the total number of irradiating protons. The time resolution was evaluated also as functions of the hit position and the energy deposition.

We observed a time resolution of approximately 75 ps for minimum ionizing particles, which further improved to around 45 ps with increasing the energy deposition. The detector maintained stable performance under high-rate conditions up to 1.35 MHz per slat, with no significant deterioration in both the amplitude and timing response. Radiation-induced degradation of the signal amplitude was observed, particularly for MPPCs located near the reaction target, with a reduction of approximately 35% at an estimated 1 MeV neutron-equivalent fluence of $2.4 \times 10^{10}~{\rm cm}^{-2}$. A slight deterioration in time resolution

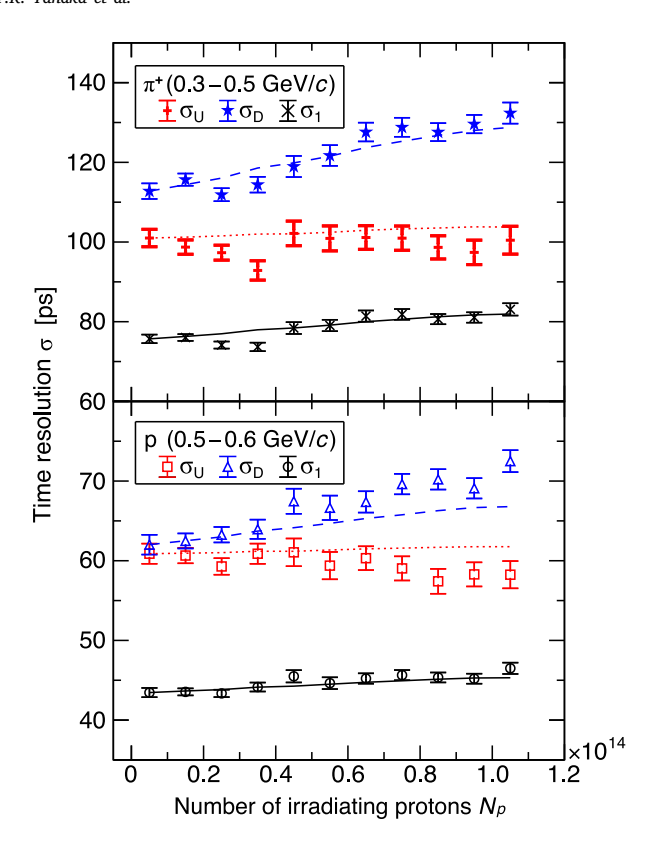


Fig. 13. Evaluated time resolutions as functions of the total number of irradiating protons, N_p . The dotted, dashed, and solid curves present estimated trends, assuming that the deterioration of the time resolution was caused as a consequence of the QDC reduction.

was also observed, which can be attributed to a consequence of the amplitude reduction.

These results demonstrate the overall performance of the MPPC-based plastic scintillator system under realistic experimental conditions with hadronic beams, including high counting rates and radiation exposure, and would serve as a reference for the design and developments of future experiments with similar experimental conditions and requirements.

CRediT authorship contribution statement

Y.K. Tanaka: Writing - review & editing, Writing - original draft, Visualization, Supervision, Software, Methodology, Investigation, Formal analysis, Conceptualization. R. Sekiya: Writing - review & editing, Writing - original draft, Visualization, Software, Methodology, Investigation, Formal analysis, Conceptualization. K. Itahashi: Writing review & editing, Writing - original draft, Supervision, Methodology, Investigation, Formal analysis, Conceptualization. H. Alibrahim Alfaki: Writing - review & editing, Methodology. F. Amjad: Writing review & editing, Methodology. M. Armstrong: Writing - review & editing, Methodology. K.-H. Behr: Writing - review & editing, Methodology. J. Benlliure: Writing - review & editing, Methodology. Z. Brencic: Writing - review & editing, Methodology. T. Dickel: Writing - review & editing, Methodology. V. Drozd: Writing - review & editing, Methodology, Conceptualization. S. Dubey: Writing - review & editing, Methodology. H. Ekawa: Writing - review & editing, Methodology. S. Escrig: Writing - review & editing, Methodology. M. Feijoo-Fontán: Writing – review & editing, Methodology. H. Fujioka: Writing - review & editing, Methodology, Conceptualization. Y. Gao: Writing - review & editing, Methodology. H. Geissel: Writing - review & editing, Methodology. F. Goldenbaum: Writing - review & editing, Methodology. A. Graña González: Writing – review & editing, Methodology. E. Haettner: Writing - review & editing, Methodology. M.N. Harakeh: Writing - review & editing, Methodology. Y. He: Writing - review & editing, Methodology. H. Heggen: Writing - review & editing, Methodology. C. Hornung: Writing - review & editing, Methodology. N. Hubbard: Writing – review & editing, Methodology. M. Iwasaki: Writing - review & editing, Methodology. N. Kalantar-Nayestanaki: Writing - review & editing, Methodology. A. Kasagi: Writing - review & editing, Methodology. M. Kavatsyuk: Writing - review & editing, Methodology. E. Kazantseva: Writing - review & editing, Methodology. A. Khreptak: Writing - review & editing, Methodology. B. Kindler: Writing – review & editing, Methodology. H. Kollmus: Writing - review & editing, Methodology. D. Kostyleva: Writing - review & editing, Methodology. S. Kraft-Bermuth: Writing - review & editing, Methodology. N. Kurz: Writing - review & editing, Methodology. E. Liu: Writing - review & editing, Methodology. B. Lommel: Writing - review & editing, Methodology. S. Minami: Writing - review & editing, Methodology. D.J. Morrissey: Writing - review & editing, Methodology. P. Moskal: Writing - review & editing, Methodology. I. Mukha: Writing - review & editing, Methodology. M. Nakagawa: Writing - review & editing, Methodology. C. Nociforo: Writing - review & editing, Methodology. H.J. Ong: Writing - review & editing, Methodology. S. Pietri: Writing - review & editing, Methodology. S. Purushothaman: Writing - review & editing, Methodology. C. Rappold: Writing – review & editing, Software, Methodology. E. Rocco: Writing - review & editing, Methodology. J.L. Rodríguez-Sánchez: Writing - review & editing, Methodology. P. Roy: Writing - review & editing, Methodology. R. Ruber: Writing - review & editing, Methodology. T.R. Saito: Writing - review & editing, Methodology, Conceptualization. S. Schadmand: Writing review & editing, Methodology. C. Scheidenberger: Writing - review & editing, Methodology. P. Schwarz: Writing - review & editing, Methodology. V. Serdyuk: Writing - review & editing, Methodology. M. Skurzok: Writing - review & editing, Methodology. B. Streicher: Writing - review & editing, Methodology. K. Suzuki: Writing - review & editing, Methodology, Conceptualization. B. Szczepanczyk: Writing - review & editing, Methodology. X. Tang: Writing - review & editing, Methodology. N. Tortorelli: Writing - review & editing, Methodology. M. Vencelj: Writing – review & editing, Methodology. T. Weber: Writing - review & editing, Methodology. H. Weick: Writing - review & editing, Methodology. M. Will: Writing - review & editing, Methodology. K. Wimmer: Writing - review & editing, Methodology. A. Yamamoto: Writing - review & editing, Methodology. A. Yanai: Writing - review & editing, Methodology. J. Zhao: Writing - review & editing, Methodology.

Declaration of competing interest

The authors declare that they have no known competing financial interests or personal relationships that could have appeared to influence the work reported in this paper.

Acknowledgments

The authors would like to acknowledge the GSI staff for their support in the experiment. The WASA-FRS experiments were performed in the framework of the FAIR Phase-0 program at GSI. This work is partly supported by JSPS Grants-in-Aid for Early-Career Scientists (Grant No. JP20K14499), for Scientific Research (B) (Grant No. JP18H01242), and for Scientific Research (A) (Grant No. JP24H00238) and JSPS Fostering Joint International Research (B) (Grant No. JP20KK0070). The authors would like to acknowledge supports from the SciMat and qLife Priority Research Areas budget under the program Excellence Initiative-Research University at the Jagiellonian University, Poland, from Proyectos I+D+i 2020 (ref: PID2020-118009GA-I00),

from the program 'Atracción de Talento Investigador' of the Community of Madrid, Spain (Grant 2019-T1/TIC-131), from the Regional Government of Galicia under the Postdoctoral Fellowship, Spain Grant No. ED481D-2021-018, the MCIN, Spain under Grant No. RYC2021-031989-I, from the ExtreMe Matter Institute EMMI at the GSI Helmholtzzentrum für Schwerionenforschung, Darmstadt, Germany, and from the European Union's Horizon 2020 research and innovation programme (Grant No. 824093).

Data availability

Data will be made available on request.

References

- [1] P.W. Cattaneo, et al., IEEE Trans. Nucl. Sci. 61 (2014) 2657.
- [2] P.W. Cattaneo, et al., Nucl. Instrum. Methods Phys. Res. A 828 (2016) 191.
- [3] A. Stoykov, R. Scheuermann, K. Sedlak, Nucl. Instrum. Methods Phys. Res. A 695 (2012) 202.
- [4] M. Nishimura, et al., Nucl. Instrum. Methods Phys. Res. A 958 (2020) 162785.
- [5] A. Korzenev, et al., JPS Conf. Proc. 27 (2019) 011005.
- [6] A. Alici, et al., J. Instrum. 13 (2018) P09012.
- [7] R. Onda, et al., Nucl. Instrum. Methods Phys. Res. A 936 (2019) 563.
- [8] E. Garutti, Yu. Musienko, Nucl. Instrum. Methods Phys. Res. A 926 (2019) 69.
- [9] Y. Qiang, et al., Nucl. Instrum. Methods Phys. Res. A 698 (2013) 234.
- [10] V. Mikhaylov, et al., J. Instrum. 15 (2020) C02005.
- [11] A. Heering, et al., Nucl. Instrum. Methods Phys. Res. A 824 (2016) 111.
- [12] K. Ieki, et al., Nucl. Instrum. Methods Phys. Res. A 1053 (2023) 168365.

- [13] S. Sánchez Majos, et al., Nucl. Instrum. Methods Phys. Res. A 602 (2009) 506.
- [14] E. Garutti, et al., arXiv:1709.05226 [physics.ins-det].
- [15] M. Yu. Barnyakov, et al., Nucl. Instrum. Methods Phys. Res. A 824 (2016) 83.
- [16] R. Sekiya, et al., Nucl. Instrum. Methods Phys. Res. A 1034 (2022) 166745.
- [17] C. Bargholtz, et al., Nucl. Instrum. Methods Phys. Res. A 594 (2008) 339.
- $[18] \ \ \text{H.-H. Adam, et al., WASA-at-COSY Collaboration, } \\ \text{arXiv:nucl-ex/0411038.}$
- [19] Y.K. Tanaka, et al., Acta Phys. Pol. B Proc. Suppl. 16 (2023) 4-A27.
- [20] T.R. Saito, et al., Nucl. Instrum. Methods Phys. Res. B 542 (2023) 22.
- [21] Y.K. Tanaka, et al., J. Phys. Conf. Ser. 1643 (2020) 012181.
- [22] R. Sekiya, et al., arXiv:2509.07824 [nucl-ex].
- [23] T.R. Saito, et al., Nat. Rev. Phys. 3 (2021) 803.
- [24] H. Geissel, et al., Nucl. Instrum. Methods Phys. Res. B 70 (1992) 286.
- [25] Y.K. Tanaka, et al., Phys. Rev. C 97 (2018) 015202.
- [26] N. Ikeno, et al., arXiv:2406.06058 [nucl-th].
- [27] Y.K. Tanaka, et al., Phys. Rev. Lett. 117 (2016) 202501.
- [28] M. Jacewicz, Ph.D. thesis, Uppsala University, 2004.
- [29] R.J.M.Y. Ruber, et al., Nucl. Instrum. Methods Phys. Res. A 503 (2003) 431.
- [30] I. Koch, Ph.D. thesis, Uppsala University, 2004.
- [31] B. Jurado, K.-H. Schmidt, K.-H. Behr, Nucl. Instrum. Methods Phys. Res. A 483
- [32] A. Codino, Nucl. Instrum. Methods Phys. Res. A 440 (2000) 191.
- [33] M. Ohlsson, C. Peterson, A.L. Yuille, Comput. Phys. Comm. 71 (1992) 77.
- [34] C. Höppner, et al., Nucl. Instrum. Methods Phys. Res. A 620 (2010) 518.
- [35] R. Sekiya, in preparation for Ph.D. thesis, Kyoto University.
- [36] S. Agostinelli, et al., Nucl. Instrum. Methods Phys. Res. A 506 (2003) 250.
- [37] J. Allison, et al., Nucl. Instrum. Methods Phys. Res. A 835 (2016) 186.
- [38] G. Lindström, Nucl. Instrum. Methods Phys. Res. A 512 (2003) 30.
- [39] ASTM E722-19, Standard Practice for Characterizing Neutron Fluence Spectra in Terms of an Equivalent Monoenergetic Neutron Fluence for Radiation Hardness Testing of Electronics, ASTM International, 2019.